



Model-potential method for high-order harmonic generation in monolayer graphene

Xin-Qiang Wang ^{1,2} and Xue-Bin Bian ^{1,*}

¹State Key Laboratory of Magnetic Resonance and Atomic and Molecular Physics, Wuhan Institute of Physics and Mathematics, Innovation Academy for Precision Measurement Science and Technology, Chinese Academy of Sciences, Wuhan 430071, China

²University of Chinese Academy of Sciences, Beijing 100049, China



(Received 29 October 2019; accepted 23 March 2021; published 7 May 2021)

We develop a model potential to simulate the effective potential of a single active electron in monolayer graphene by taking the electron energy band structure calculated by the density functional theory (DFT) as a reference. Based on the single-electron Schrödinger equation, the model potential is used to calculate not only the energy band structure but also the transition dipole moment, charge density, and other physical quantities of graphene. These quantities are compared with results from DFT and a good consistency is achieved. The simulation of laser-graphene interaction with the same laser parameters as Yoshikawa *et al.* [*Science* **356**, 736 (2017)] is performed with the time-dependent Schrödinger equation. The obtained driving laser ellipticity scaling, the harmonic ellipticity, and the harmonic major-axis angle can well reproduce the experimental results. It is found that the carrier-envelope phase and chirp effects are capable of regulating high-order harmonic generation in monolayer graphene. The model potential method can be extended to field-free calculations and dynamic simulations in other materials as long as the corresponding model potential is constructed.

DOI: [10.1103/PhysRevA.103.053106](https://doi.org/10.1103/PhysRevA.103.053106)

I. INTRODUCTION

At present, the simulation of the interaction between laser and real solid materials is mainly realized by solving semiconductor Bloch equations (SBEs) [1–4] and time-dependent density functional theory (TDDFT) [5–9]. The time-dependent Schrödinger equation (TDSE) is mainly used in model solids [10–12] which cannot represent real solid materials. The SBE method needs a precalculated band structure and transition dipole moment, which are typically calculated by density functional theory (DFT). The DFT method produces accurate relative energy. But the calculation of the transition dipole phase introduces meaningless values for different k points, because different iteration steps are needed to get a convergent energy at different k points and in every iteration of the Kohn-Sham (KS) equations only the modulus of the wave function is retained and no constraints and connections between different k points are added to wave function phase calculation. The DFT generates discontinuous eigenwave-function phases. Because the SBE in the length gauge contains the derivative of an eigenwave function with respect to k , the SBE cannot be directly solved based on the eigenwave function with discontinuous phases. The treatment of dipole phases has been proposed in Refs. [13–17]. The TDDFT method is very time consuming, even using lots of computing resources. It usually needs large memory and is difficult to be applied in large system simulations [18]. But, if time-dependent electron-electron interaction is strong, TDDFT is still a good choice.

We have developed a model potential method for real monolayer graphene which is based on the time-dependent

Schrödinger equation and basis expansion techniques. The accuracy of an eigenenergy from a model potential is usually worse than that from the pseudopotential mostly used in DFT and TDDFT calculations. Usually it is difficult to accurately obtain the band structure and other information about crystals using the model potential. But our model potential has been optimized to be sufficiently accurate for both field-free and field-driven conditions. Comparisons of our calculations with DFT and experimental results will be shown in the following text.

The TDSE calculation starts from the potential which contains the material structure. It is not necessary to modify the phase of the eigenstate as well as the phase of the dipole in the TDSE calculation. The problem of phase discontinuity of the eigenwave function is introduced in the calculation of the diagonalization of the Hamiltonian matrix. At the potential level, the problem itself does not exist. The model potential method can be applied in both reciprocal space and real space in which inhomogeneous field effects can be taken into consideration. We go into formalism details about field-free graphene in Sec. II and laser-irradiated graphene in Sec. III. A brief summary is given in Sec. IV.

II. FIELD-FREE CALCULATIONS OF PHYSICAL QUANTITIES OF GRAPHENE

The time-independent Schrödinger equation (TISE),

$$\hat{H}_0|\phi_n\rangle = E_n|\phi_n\rangle, \quad (1)$$

is solved to get the eigenstates $|\phi_n\rangle$ and eigenvalues E_n of monolayer graphene, where the field-free Hamiltonian is

$$\hat{H}_0 = \frac{\hat{p}^2}{2} + V(\vec{r}). \quad (2)$$

*xuebin.bian@wipm.ac.cn

Atomic units are used throughout the paper unless stated otherwise. Inspired by the band-structure calculation work [19,20], we construct a two-dimensional periodic potential for monolayer graphene whose bond length, the distance between two nearest-neighbor carbon atoms, is $R = 0.142$ nm. If $\sqrt{(x - x_c)^2 + (y - y_c)^2} < 0.41R$,

$$V(x, y) = -a_v \exp\{-b_v[(x - x_c)^2 + (y - y_c)^2]\}, \quad (3)$$

where $a_v = 1.901$, $b_v = 2.84648$, (x_c, y_c) is the coordinate of a carbon atom, and $V(x, y) = 0$ elsewhere.

We expand the eigenstates with basis functions by means of which matrix elements of the Hamiltonian are also calculated. The orthonormal basis function in the x direction under coordinate representation is taken, according to the Bloch theorem, as

$$\langle x | \psi_{i_x} \rangle = \frac{1}{\sqrt{a_x}} \exp(ik_x x) u_{n_x}(x), \quad (4)$$

where i_x is the integer index of the basis function ($i_x = 1, 2, 3, \dots$), k_x is the quasimomentum, and u_{n_x} is a spatial periodic function

$$u_{n_x}(x \pm a_x) = u_{n_x}(x), \quad (5)$$

where a_x denotes the spatial period (length of the unit cell) in the x direction. We assume $u_{n_x}(x)$ to be

$$u_{n_x}(x) = \exp(in_x \omega_x x), \quad (6)$$

where $\omega_x = \frac{2\pi}{a_x}$ depicts the spatial frequency of the periodic potential in the x direction. $\frac{1}{\sqrt{a_x}}$ normalizes the basis function and ensures that

$$\langle \psi_m | \psi_j \rangle = \delta(m - j) = \begin{cases} 1 & (m = j) \\ 0 & (m \neq j). \end{cases} \quad (7)$$

N_x basis functions are used in the x direction. We recommend an odd number for N_x so the constant basis ($n_x = 0$) and symmetric bases ($n_x = \pm n$) are included. The relation connecting i_x , n_x , and N_x is $n_x = i_x - \frac{N_x+1}{2}$ in the case that N_x is odd. This set of bases is sufficient for one-dimensional systems.

When the system is two dimensional which is just the case for monolayer graphene, an additional set of bases should be introduced. The y -direction basis function is

$$\langle y | \psi_{i_y} \rangle = \frac{1}{\sqrt{a_y}} \exp(ik_y y) u_{n_y}(y). \quad (8)$$

For every property and relation stated about $|\psi_{i_x}\rangle$, there is an analog for the orthonormal basis in the y direction. The direct product of the basis vectors in the x and y directions generates two-dimensional basis vectors and their combination is flexible and changeable. One formalism of two-dimensional basis set is recommended as follows:

$$\begin{aligned} |\Psi_1(x, y)\rangle &= |\psi_1(x)\psi_1(y)\rangle, \\ |\Psi_2(x, y)\rangle &= |\psi_1(x)\psi_2(y)\rangle, \\ |\Psi_3(x, y)\rangle &= |\psi_1(x)\psi_3(y)\rangle, \dots, \end{aligned} \quad (9)$$

in which case there are many published processing functions to handle the generated two-dimensional array. The l th two-

dimensional basis vector can be expressed as

$$\begin{aligned} \langle r | \Psi_l(x, y) \rangle &= \langle r | \psi_{i_x}(x) \psi_{i_y}(y) \rangle \\ &= \frac{1}{\sqrt{a_x a_y}} \exp \left[i \left(n_x \frac{2\pi}{a_x} + k_x \right) x + i \left(n_y \frac{2\pi}{a_y} + k_y \right) y \right]. \end{aligned} \quad (10)$$

Then matrix elements that constitute the time-independent Hamiltonian turn out to be

$$\begin{aligned} \langle \Psi_k(x, y) | \frac{\hat{p}^2}{2} | \Psi_l(x, y) \rangle &= \frac{1}{2} \left[\left(\frac{2\pi n_x}{a_x} + k_x \right)^2 + \left(\frac{2\pi n_y}{a_y} + k_y \right)^2 \right] \\ &\times \delta(i_x - j_x) \delta(i_y - j_y) \end{aligned} \quad (11)$$

and

$$\begin{aligned} \langle \Psi_k(x, y) | V | \Psi_l(x, y) \rangle &= \frac{1}{a_x a_y} \iint dx dy V \exp \left[i \frac{2\pi(i_x - j_x)}{a_x} x \right. \\ &\left. + i \frac{2\pi(i_y - j_y)}{a_y} y \right], \end{aligned} \quad (12)$$

where

$$|\Psi_k(x, y)\rangle = |\psi_{j_x}(x) \psi_{j_y}(y)\rangle. \quad (13)$$

Solving Eqs. (1), (2), (11), and (12), we can obtain the eigenvalues and eigenstates that are cornerstones for calculating the graphene band structure, dipole, and charge density.

The spatial structure and unit cell of monolayer graphene are shown in Fig. 1(a). Lengths of two sides of the unit cell are $a_x = \sqrt{3}R$ and $a_y = 3R$. According to the symmetry of the Brillouin zone, we designate, in Fig. 1(b), a high-symmetry path as Γ - X' - M - X - D - Γ - M . If necessary, the energy bands can be transformed into a hexagonal Brillouin zone from the rectangular one by quantum unfolding [21]. The band structure along the selected path is calculated by solving Eq. (1) and is displayed in Fig. 1(c). The carbon atom Perdew-Burke-Ernzerhof pseudopotential is used in the Vienna *Ab initio* Simulation Package (VASP) to compute energy bands that are shown in Fig. 1(d) to verify the band structure from our model potential. A high consistency is achieved in results from TISE [Fig. 1(c)] and DFT [Fig. 1(d)], especially those near the Dirac point (zero energy) that are precisely the energy bands which play a major role in the field-driven electron dynamics.

Transition dipole moments, which are calculated by

$$\vec{d}_{m,n} = \frac{i}{E_n - E_m} \langle \phi_m | \hat{p} | \phi_n \rangle, \quad (14)$$

largely determine the strength of the interband transition process of electrons. The x - and y -direction components of transition dipole moments between the state n (the first band above zero energy) and the state m (the first band below zero energy) are separately presented in Figs. 2(a) and 2(b). TISE and DFT results agree well in both directions. Their absolute values are different, as different normalization techniques are performed on eigenstates. In TISE, the basis-expansion coefficient matrix of an eigenstate is normalized. And then, the normalized eigenstates are used to calculate transition

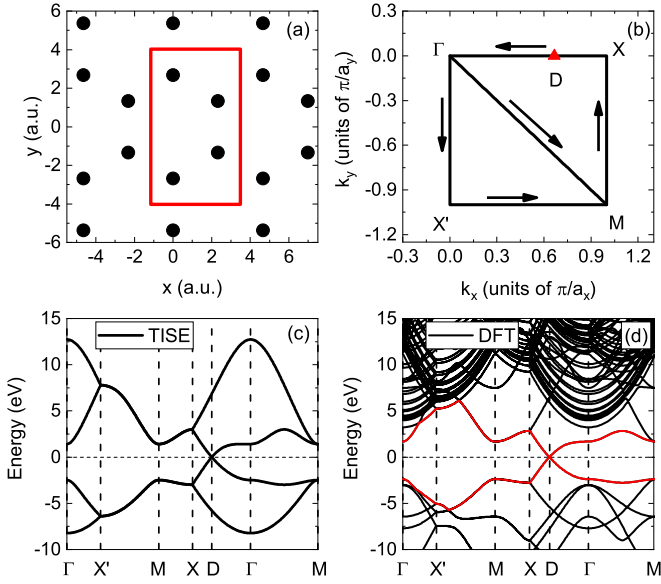


FIG. 1. Band structure of monolayer graphene. (a) A sketch of graphene honeycomb lattice. Solid black circles represent carbon atoms. The rectangle area surrounded by the solid red line is the unit cell used through this article. (b) The high-symmetry path in part of the first Brillouin zone. The red triangle indicates the zero-gap Dirac point. The band structure has been calculated by (c) TISE and (d) DFT. Vertical dashed lines in (c) and (d) correspond to high-symmetry points presented in (b). The energy bands closest to zero are marked in red in (d).

dipoles. However, what really matters is their relative values in different k points that already match.

The charge distribution is further computed and displayed in Fig. 3 to confirm that TISE and DFT results can coincide with each other even in a single k -point eigenstate. 101×101 k points are used in the DFT static self-consistent calculation for the band structure, dipole, and charge density. The accuracy of eigenvalues and eigenstates ensures that we can accurately obtain almost all the unperturbed physical properties of graphene, which means that the model potential we constructed is sufficient to simulate the real single-layer graphene.

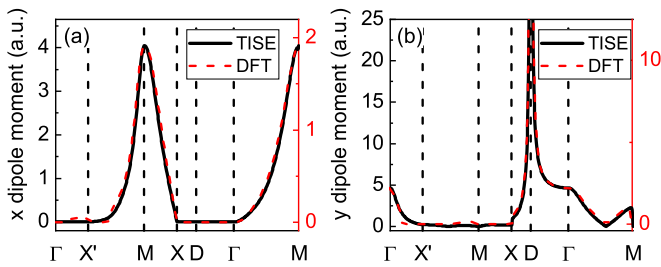


FIG. 2. Absolute values of transition dipoles in the high-symmetry path. Components of transition dipoles in (a) x and (b) y directions. Dipole amplitudes from TISE method (solid black lines) are compared with those from DFT calculations (red dashed lines). The longitudinal coordinates on the left-hand side in (a) and (b) correspond to TISE, while the right-hand-side ones in red correspond to DFT.

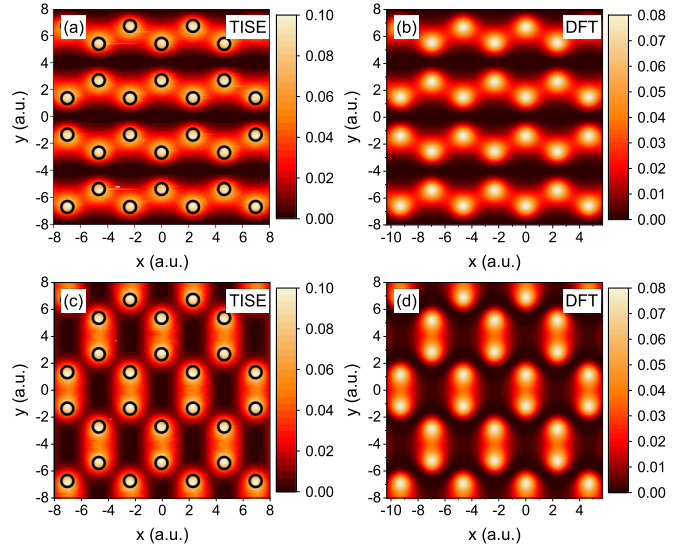


FIG. 3. Single k -point charge distribution of monolayer graphene. Charge densities of two adjacent eigenstates around zero energy at D , the Dirac point marked in Fig. 1(b), are exhibited in (a) and (b) (below zero energy) and (c) and (d) (above zero energy). Carbon atoms are indicated by open black circles in TISE results [(a) and (c)]. They are omitted in the DFT outcomes [(b) and (d)] because they are in exactly the same place visually. But the coordinates of carbon atoms are different because the origin of the coordinates is shifted in the DFT calculation.

III. LASER-GRAPHENE INTERACTION

The laser-graphene interaction is simulated by numerically solving the two-dimensional TDSE within the dipole approximation in the velocity gauge:

$$i \frac{\partial \psi(\vec{r}, t)}{\partial t} = \left(\frac{\hat{p}^2}{2} + V(\vec{r}) + \vec{A}(t) \cdot \hat{p} \right) \psi(\vec{r}, t), \quad (15)$$

where \vec{A} is the magnetic vector potential and $\vec{A}(t) = -\int \vec{E}(t) dt$. The elliptically polarized field $\vec{E}(t)$ is defined as

$$\begin{cases} E_x = \frac{1}{\sqrt{1+\varepsilon^2}} E_0 f(t) \cos(\omega_0 t + \varphi) \\ E_y = -\frac{\varepsilon}{\sqrt{1+\varepsilon^2}} E_0 f(t) \sin(\omega_0 t + \varphi), \end{cases} \quad (16)$$

where E_x and E_y are the x and y components of the laser field, respectively. ε , E_0 , ω_0 , and φ separately correspond to the laser ellipticity, electric field strength, laser angular frequency, and the carrier-envelope phase (CEP). The envelope function is portrayed as $f(t) = \exp(-2 \ln 2 t^2 / \tau^2)$, where τ is related to the full width at half maximum (FWHM). The definition of screw is in accordance with the traditional terminology that is also used in Born's book [22]: $\varepsilon < 0$ corresponds to a left-handed polarized field, and $\varepsilon > 0$ corresponds to right-handed polarization. The electric field has a strength of 30 MV/cm, single photon energy of 0.26 eV, FWHM of 25 fs, and five-cycle duration.

We assume that the Fermi level is zero before the pump pulse arrives and that electrons are distributed all over the valence band below the Fermi level. 101×101

quasimomentum k points at equal intervals are sampled in the valence band. The TDSE is solved in each k point independently [10]. But the spatially inhomogeneous fields will induce couplings between different crystal momenta. In the inhomogeneous-field case, we can solve the TDSE in real space in the length gauge. The initial state in real space can be formed by adding different k eigenstates together. The couplings between different k points will be naturally contained in the time-evolution process in real space. The Crank-Nicolson method [11,23,24],

$$\begin{aligned} & \left(1 + i\frac{\Delta t}{2}\hat{H}\left(t + \frac{\Delta t}{2}\right)\right)|\psi(\vec{r}, t + \Delta t)\rangle \\ &= \left(1 - i\frac{\Delta t}{2}\hat{H}\left(t + \frac{\Delta t}{2}\right)\right)|\psi(\vec{r}, t)\rangle, \end{aligned} \quad (17)$$

is used to propagate the time-dependent wave function with 1024×4 time steps per optical cycle. The electron wave function is expanded with basis vectors defined in Eq. (10). And then, currents can be calculated as

$$j_x(t) = \langle\psi(t)|\hat{p}_x|\psi(t)\rangle \quad (18)$$

and

$$j_y(t) = \langle\psi(t)|\hat{p}_y|\psi(t)\rangle. \quad (19)$$

The harmonic emission intensity is obtained from the Fourier transform of these laser-induced currents:

$$S_x(\omega) = \left|\int j_x(t)\exp(-i\omega t)dt\right|^2 \quad (20)$$

and

$$S_y(\omega) = \left|\int j_y(t)\exp(-i\omega t)dt\right|^2. \quad (21)$$

We also calculate the laser-ellipticity dependence of high-order harmonic generation (HHG) in graphene. Similar results are obtained with Yoshikawa *et al.*'s experiment [25] and presented in Figs. 4(a) and 4(b). With the increase of the ellipticity of driving light, the harmonic intensity in the x direction decreases gradually. However, the harmonic intensity in the y direction increases first and then decreases, and the maximum appears at a certain ellipticity. In the experimental results, the maximum y component is larger than the maximum x component for the seventh harmonic but smaller than the maximum x component for the fifth harmonic. The y -direction maximum of the seventh harmonic does not exceed the maximum value in the x direction in the TDSE results. They are almost of the same size. This difference should be attributed to the time-dependent electron-electron interaction which should be calculated with TDDFT or the dephasing time which can be phenomenologically added in the SBE. The TDSE results of the fifth harmonic show a good consistency with the experiment. With the increase of harmonic order, the maximum intensity of the y -direction harmonic increases relative to the maximum intensity of the x -direction harmonic in the experiment. The TDSE results can well reproduce this trend.

The detailed harmonic elliptical properties including harmonic ellipticity and harmonic major axis orientation angle are extracted with the method in Refs. [22,26] and shown

in Figs. 4(c) and 4(d) for the linear driving pulse, and in Figs. 4(e) and 4(f) for the pump light ellipticity of 0.3. A linear pump pulse generates linearly polarized harmonics and their polarization direction is parallel to the driving light, as is shown in Figs. 4(c) and 4(d). But for the case where the ellipticity of the driving light is 0.3 [Figs. 4(e) and 4(f)], different harmonics show different properties. The fifth and seventh harmonics have close ellipticities around 0.2, which is almost the same as Yoshikawa *et al.*'s experiment [25]. The fifth harmonic is left-handed polarized while the seventh one is on the opposite and this is not distinguished experimentally. Their polarization direction no longer follows the polarization axis of the driving laser. The harmonic major axis orientation angle is found at around 130° for the fifth harmonic and 110° for the seventh harmonic, which is also in good coincidence with Yoshikawa *et al.*'s results [25].

Graphene is expected to play an important role in electronic and optical devices owing to its excellent mechanical, electrical, and optical properties. Therefore, the optical response of graphene deserves extensive studies. CEP has been demonstrated to be able to effectively regulate harmonic generation in semiconductors [27], especially harmonics with relatively higher energy where interband contribution dominates. We find that the CEP of a linearly polarized field along the x axis can also regulate HHG in graphene that has a zero-gap band structure. The seventh and the ninth harmonics in the pump pulse with a CEP of 0.5π are shifted to lower frequencies compared with those in the field with a CEP of zero, which is shown in Fig. 5(a). But harmonics lower than the seventh order hardly change with the variation of CEP. We increased the light intensity to 1.15 times stronger, and similar results still exist. Although the shift is not very large, this implies that interband contribution has significant effects in graphene, especially on harmonics above the seventh order.

The chirped electric field is defined as

$$A(t) = -E_0/\omega_0 \sin \left[\omega_0(t - t_d/2) + \alpha_c \left(\frac{t - \tau_0}{600} \right)^2 \right] f(t), \quad (22)$$

where t_d is the pulse duration, α_c is the chirp parameter, and τ_0 is $1/3$ if $\alpha_c \geq 0$ or $2/3$ if $\alpha_c < 0$. The chirp has little effect on the intensity of the harmonic emission which is presented in Fig. 5(b). For visual clarity, the red line is multiplied by 10^3 , and the green and black lines are multiplied by 10^{-3} . Many noninteger harmonics arise in the harmonic emission under the chirp parameters of 0.5 and -0.5 , resulting in a multiplex spectrum. As the chirp amplitude continues to increase, near-continuous spectra appear when chirp parameters are 1 and -1 . To have a deep insight into the underlying radiation mechanism, time-frequency analyses are performed on the laser-induced currents by means of wavelet transform [28–30]. Time profiles of HHG for different chirp parameters are exhibited in Figs. 5(c)–5(e), from which we can see harmonic radiation channels follow electric field peaks. Under the pump pulse without chirp, intensities and times of emission are nearly symmetric about the center of the pulse duration. This symmetry, together with a half-cycle emission period, generates odd-order harmonics. The introduced laser chirp shifts emission times in the temporal domain and breaks the time symmetry and periodicity of spectral and tempo-

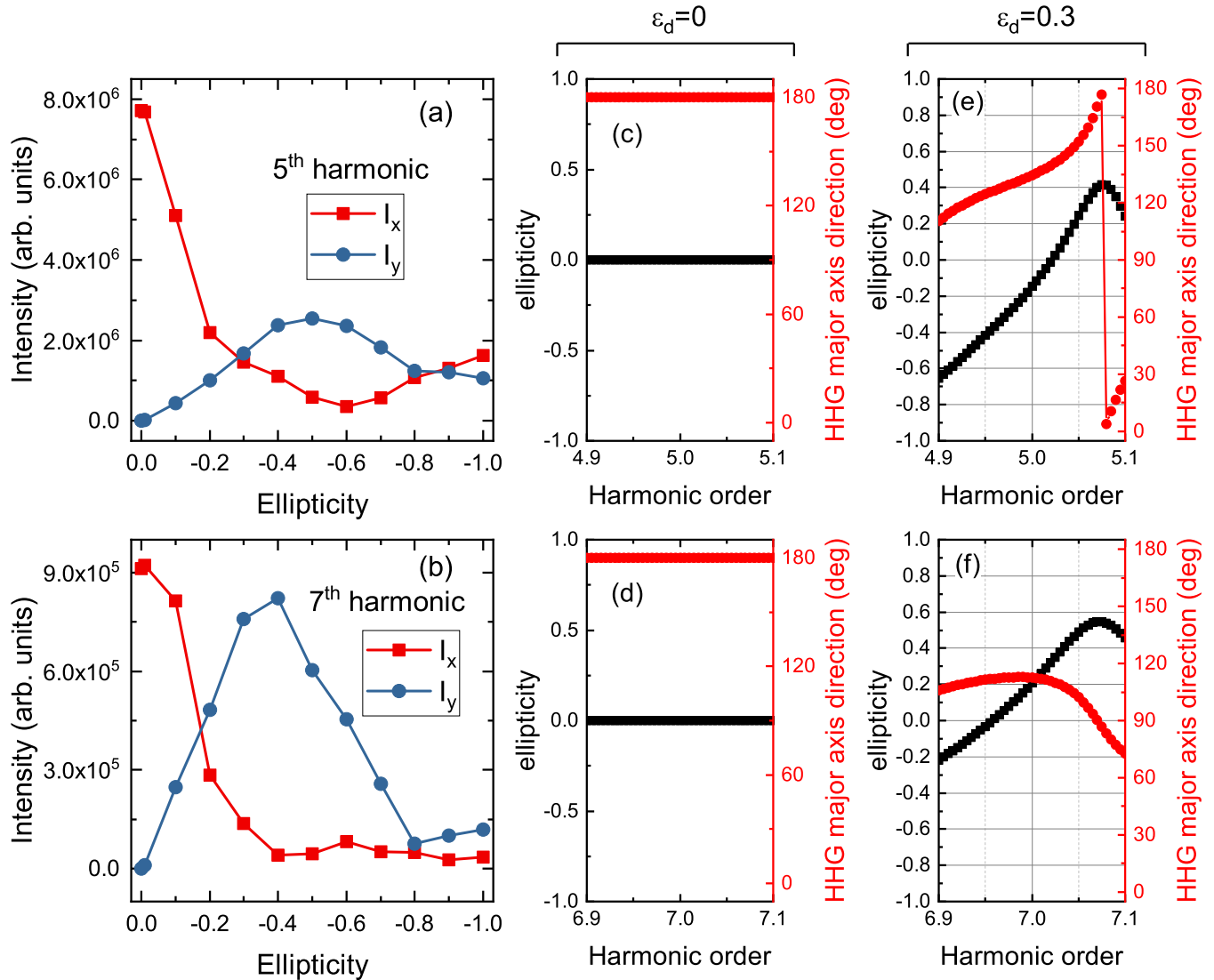


FIG. 4. Laser ellipticity dependence of HHG in graphene and the generated harmonic ellipticity. (a) The pump pulse ellipticity dependence of the fifth high harmonic. (c) Under the linearly polarized driving pulse ($\epsilon_d = 0$), the generated fifth harmonic ellipticity and its major axis orientation angle of the electric vector ellipse are shown. The same physical quantities are presented in (e) except that the ellipticity of the driving light is 0.3. Panels (b), (d), and (f) correspond to (a), (c), and (e), respectively, but for the seventh harmonic.

ral structures [Figs. 5(c)–5(e)]; then noninteger harmonics emerge. With the increasing chirp amplitude, the asymmetric and aperiodic harmonic radiation times increase, more and more noninteger harmonics appear, and then the harmonic spectrum begins to approach a continuum spectrum.

With the increase of the amplitude of chirp parameter, blueshifts occur in the harmonic spectrum. The blueshift is partly because of an increase in the frequency of the driving pulse, as can be seen in Fig. 5(b). What makes more sense is that the blueshifts caused by the up chirp and the down chirp are different, and the difference grows with the increasing chirp amplitude. Especially when the absolute value of chirp parameter is taken as one, the frequency-shift difference of the third harmonic under up-chirp and down-chirp pulses can even exceed one photon energy, which can be observed clearly in experiments. The blueshift of negative chirp is larger than that of positive chirp. According to the definition of the chirped pulse, the up-chirp pulse and the down-chirp pulse are

just flipped about the center of time duration. Time-frequency analyses of pulses with the same chirp size but different chirp signs will reveal that the frequency distribution of pulse is also flipped in the temporal domain when the sign of the chirp parameter alters. Fourier transforms of the two pulses produce the same spectrum. Then how does the difference of blueshift come about, for example, when the chirp is 0.5 or -0.5 ? An additional asymmetrical process is needed to generate this blueshift difference. The excitation process of electrons is a natural one. It is affected by the excitation passages and the number of electrons. Without considering the influence of electron population on energy band, the distortion of the energy band is almost the same under the same laser frequency and intensity according to the Floquet-Bloch method [31], and hence the electron excitation passage would be the same in the same laser parameters. Because the electric field of $\alpha_c = 0.5$ coincides with the field of $\alpha_c = -0.5$ when the electric field is flipped in time, the electron excitation passage

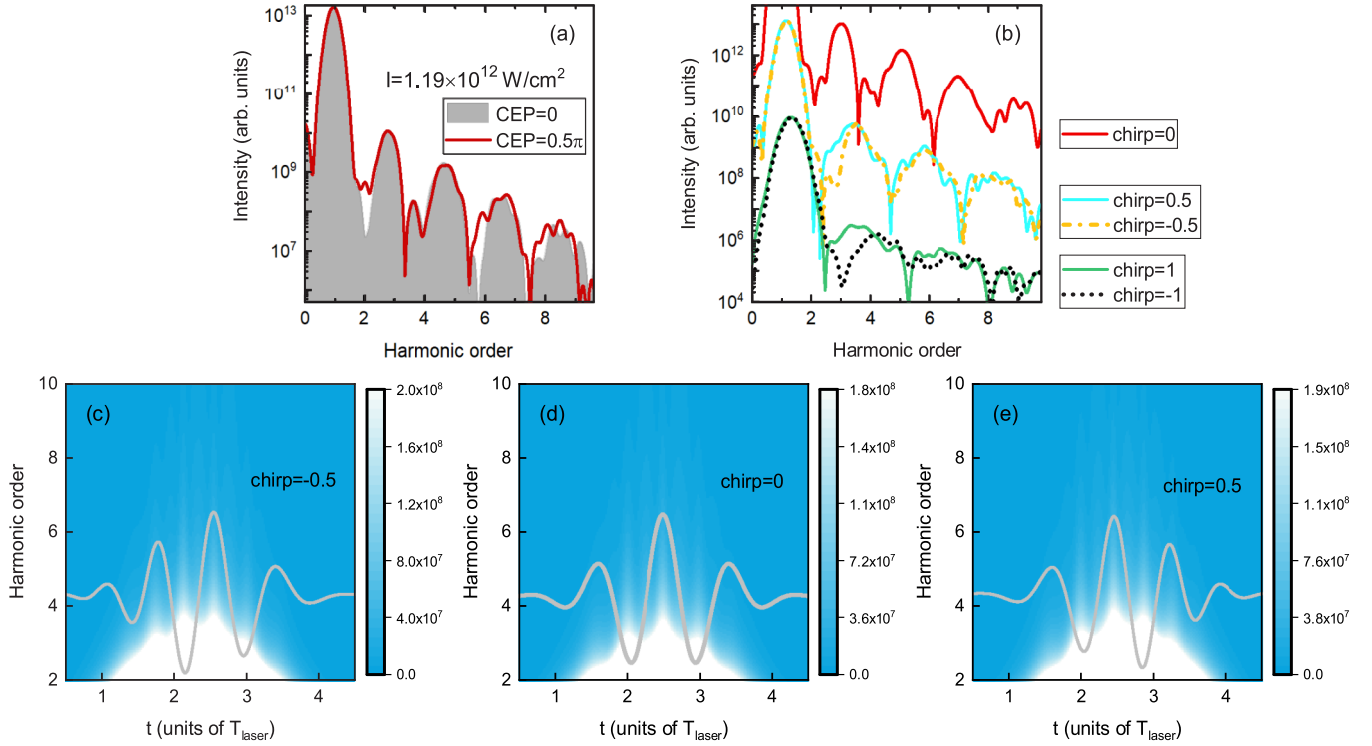


FIG. 5. CEP and chirp effects of high-order harmonic generation in monolayer graphene. (a) Harmonic spectra in different CEPs. The shaded area of the spectrum denotes the harmonic emission when CEP is zero. The red line spectrum corresponds to the case when CEP is 0.5π . (b) Spectra in different chirp parameters: upper red line, chirp = 0; middle cyan line, chirp = 0.5; middle yellow dot-dashed line, chirp = -0.5; lower green line, chirp = 1; and lower black dotted line, chirp = -1. Spectral and temporal emission profiles of HHG for three chirp parameters: (c) chirp = -0.5, (d) chirp = 0, and (e) chirp = 0.5. Gray lines in (c-e) represent the electric fields with corresponding chirp parameters. T_{laser} denotes the optical cycle.

in the case of $\alpha_c = 0.5$ should be the same with that in the case of $\alpha_c = -0.5$ when it is flipped in the time axis. They are symmetrical in the time domain. Under the irradiation of pulse, electrons are excited, so the number of electrons on the low-energy band gradually decreases and the number of electrons on the high-energy band increases finally. It is somewhat like the ground-state depletion process of atoms subjected to an intense laser field. It is irreversible. The depletion in atoms is usually omitted because of a large gap between the deeply bound states, but the case will be different in graphene where a zero gap exists. Because of the zero gap and band energy levels, continuous small energy gaps appear in graphene. The interband transition may happen in a wide frequency zone and over a wide time range. So the process of electron excitation in graphene is like this: For the down-chirp pulse, the former high-frequency part of the pulse interacts with graphene first and the corresponding excitation passage opens immediately. The number of electrons in the low-energy band is close to 100% now. When the latter low-frequency part of the pulse arrives, a different excitation passage opens, but now the number of electrons to be excited has been reduced significantly. For the up-chirp pulse, the process is similar. But the former low-frequency-pulse-induced excitation passage corresponds to more electron population in the low-energy band, and the latter high-frequency-pulse-induced passage corresponds to less electron population to be excited. Generally, influenced by the two factors, the symmetrical electron excitation passages and the asymmetrical low-energy-band electron

population reduction, the electron excitation processes under up-chirp and down-chirp pulses are not symmetrical in the time axis, which will greatly affect the electron intraband oscillation and interband electron-hole recombination. The ionization difference in atoms caused by opposite signs of the chirp parameter has been reported in Ref. [32]. An accurate quantitative description about the blueshift in graphene needs to include excitation passages and the acceleration theorem that is an additional part compared with atomic systems [32].

IV. SUMMARY AND CONCLUSION

In addition to the usual SBE and TDDFT methods, we have developed an electron-wave-function-based model potential method that can calculate physical properties of field-free graphene and simulate laser-graphene interaction processes including harmonic generation, excitation, and ionization of electrons. Results from DFT, an electron-density based method, are used to verify the accuracy of the potential. In addition, this method can be readily extended to other materials and three dimensional simulations. HHG from graphene driven by elliptically polarized light is computed and very similar results with the experimental work [25] are obtained under the same laser parameters. We also find that the CEP and chirp of a laser pulse can be used as fine-tuning tools for harmonic generation in graphene. Under the irradiation of the pump pulse, the time-dependent energy bands, such as the analog of adiabatic passages in atoms [32] or time-averaged

Floquet-Bloch bands [31,33], can be accomplished in this method with minor modifications.

ACKNOWLEDGMENTS

We thank Tianjiao Shao and Jia-Qi Liu for their helpful discussions. This work is supported by the National Key Research and Development program (No. 2019YFA0307702), the National Natural Science Foundation of China (NSFC) (Grants No. 91850121 and No. 11674363), and the K. C. Wong Education Foundation (GJTD-2019-15).

APPENDIX: HOW IS THE MODEL POTENTIAL CONSTRUCTED?

The Schrödinger equation of the multiple-electron system is

$$\left[-\frac{1}{2} \sum_{i=1}^N \nabla_i^2 + \sum_{i=1}^N W(\vec{r}_i) + \sum_{i=2}^N \sum_{j<i} U(\vec{r}_i, \vec{r}_j) \right] \psi = E \psi, \quad (\text{A1})$$

where $W(\vec{r}_i)$ depicts the interaction energy between one electron and all atomic nuclei, $U(\vec{r}_i, \vec{r}_j)$ defines the interaction energy between two electrons located at \vec{r}_i and \vec{r}_j , $\psi = \psi(\vec{r}_1, \vec{r}_2, \vec{r}_3, \dots, \vec{r}_N)$ is the exact electron wave function, and it contains all the coordinates of the N electrons. But this many-body problem cannot be directly solved [34]. Hohenberg, Kohn, and Sham turned this problem into a problem of a single-electron Schrödinger equation by using electron density, namely, the Kohn-Sham equation

$$\left[-\frac{1}{2} \nabla^2 + W(\vec{r}) + V_H(\vec{r}) + V_{xc}(\vec{r}) \right] \psi_i(\vec{r}) = \varepsilon_i \psi_i(\vec{r}), \quad (\text{A2})$$

where $V_H(\vec{r}) = \int \frac{n(\vec{r}')}{|\vec{r}-\vec{r}'|} d^3\vec{r}'$ is the Hartree potential, $n(\vec{r}) = 2 \sum_i \psi_i^*(\vec{r}) \psi_i(\vec{r})$ is the electron density, and $V_{xc}(\vec{r})$ is called the electron exchange and correlation term. V_{xc} contains the correction for the self-interaction contribution in the Hartree potential, electron exchange energy, electron correlation energy, and all other unknown effects [34]. The exact form of V_{xc} is unknown.

We can lump together the three interaction terms W , V_H , and V_{xc} , namely, $V = W + V_H + V_{xc}$. V is the total effective potential which is the model potential. V contains electron-nucleus interaction and electron-electron interaction and, of course, the electron exchange and correlation energy is included but it cannot be directly extracted out. By comparing Eqs. (1), (2), and (A2), we can find that the error of the model potential method will not be larger than that of the DFT method in theory. If the extraction of the electron exchange and correlation energy is necessary, we should resort

to the DFT method. In the laser-matter interaction process, the model potential method and the SBE method do not contain the time-dependent interaction between electrons which should be considered with TDDFT.

How do we get the form of the model potential? The positions of carbon atoms, namely, (x_c, y_c) , are arranged according to the spatial structure of real graphene. We use a Gaussian-type model function with parameters as the effective carbon atom potential. The parameters a_v and b_v are responsible for the height and full width at half maximum of the well, respectively. We adjust the parameters a_v and b_v to modify the shape of the potential well, which makes the band structure, eigenwave function, and transition dipole moments from the potential well agree with those of experiments and DFT calculations. With enough parameters, we can always get any type of potential [35]. The type of model function can be selected arbitrarily according to the system to be simulated. If necessary, we can always make the eigenstates get closer to the real situation by changing the function type and modifying the parameters. After getting the model potential, the 3N-dimensional problem shown in Eq. (A1) is converted into a three-dimensional problem which is like the DFT method shown in Eq. (A2).

More energy bands are obtained in the DFT calculation compared with the TISE calculation, which is shown in Figs. 1(c) and 1(d). The reason is that in the construction of the graphene model potential, we make two simplifications: (a) the effective potential energy felt by electrons at a distance from carbon atoms is zero, and (b) the potential well of a single carbon atom is isotropic. These simplifications make the case a bit like the tight-binding approximation.

The main differences between Figs. 1(c) and 1(d) lie in energy bands away from zero at points X' and Γ . However, due to the large band gap, the transition probability in this zone is relatively small. So, the additional bands have little effect on the interband dynamics of electrons. Although cross connections exist in energy bands, electrons mainly move along an energy band with the same orbits, so the extra energy bands have little effect on the intraband motion of electrons.

There are minor differences between transition dipoles of TISE and DFT results around the point X' in Figs. 2(a) and 2(b), which is because for DFT calculations, we take the two bands closest to zero in VASP [the red line in Fig. 1(d)], instead of energy bands with the same orbits [Fig. 1(c)], to calculate the transition dipole moment. But the energy gap around X' is relatively large, so the two dipoles from the closest-to-zero bands [Fig. 1(d)] and the orbit-resolved bands [Fig. 1(c)] are both close to zero. The not-yet-distinguished bands only affect the dipole results of DFT in Figs. 2(a) and 2(b) in the small zone around X' as we can see in Fig. 1(d). The model potential method is not affected in the field-free and field-driven cases.

- [1] G. Vampa, C. R. McDonald, G. Orlando, D. D. Klug, P. B. Corkum, and T. Brabec, *Phys. Rev. Lett.* **113**, 073901 (2014).
 [2] D. Golde, T. Meier, and S. W. Koch, *Phys. Rev. B* **77**, 075330 (2008).

- [3] T. Tamaya, A. Ishikawa, T. Ogawa, and K. Tanaka, *Phys. Rev. Lett.* **116**, 016601 (2016).
 [4] Y. W. Kim, T.-J. Shao, H. Kim, S. Han, S. Kim, M. Ciappina, X.-B. Bian, and S.-W. Kim, *ACS Photonics* **6**, 851 (2019).
 [5] E. Runge and E. K. U. Gross, *Phys. Rev. Lett.* **52**, 997 (1984).

- [6] T. Otobe, *Phys. Rev. B* **94**, 235152 (2016).
- [7] N. Tancogne-Dejean, O. D. Mücke, F. X. Kärtner, and A. Rubio, *Phys. Rev. Lett.* **118**, 087403 (2017).
- [8] K. Yabana, T. Sugiyama, Y. Shinohara, T. Otobe, and G. F. Bertsch, *Phys. Rev. B* **85**, 045134 (2012).
- [9] I. Floss, C. Lemell, G. Wachter, V. Smejkal, S. A. Sato, X.-M. Tong, K. Yabana, and J. Burgdörfer, *Phys. Rev. A* **97**, 011401(R) (2018).
- [10] M. Wu, S. Ghimire, D. A. Reis, K. J. Schafer, and M. B. Gaarde, *Phys. Rev. A* **91**, 043839 (2015).
- [11] Z. Guan, X. X. Zhou, and X. B. Bian, *Phys. Rev. A* **93**, 033852 (2016).
- [12] X.-Q. Wang, Y. Xu, X.-H. Huang, and X.-B. Bian, *Phys. Rev. A* **98**, 023427 (2018).
- [13] U. Lindelfelt, H.-E. Nilsson, and M. Hjelm, *Semicond. Sci. Technol.* **19**, 1061 (2004).
- [14] S. Jiang, H. Wei, J. Chen, C. Yu, R. Lu, and C. D. Lin, *Phys. Rev. A* **96**, 053850 (2017).
- [15] J. Li, X. Zhang, S. Fu, Y. Feng, B. Hu, and H. Du, *Phys. Rev. A* **100**, 043404 (2019).
- [16] L. Yue and M. B. Gaarde, *Phys. Rev. A* **101**, 053411 (2020).
- [17] S. Jiang, C. Yu, J. Chen, Y. Huang, R. Lu, and C. D. Lin, *Phys. Rev. B* **102**, 155201 (2020).
- [18] M. W. D. Hanson-Heine, M. W. George, and N. A. Besley, *Mol. Phys.* **116**, 1452 (2018).
- [19] R. L. Pavelich and F. Marsiglio, *Am. J. Phys.* **84**, 924 (2016).
- [20] G.-R. Jia, X.-Q. Wang, T.-Y. Du, X.-H. Huang, and X.-B. Bian, *J. Chem. Phys.* **149**, 154304 (2018).
- [21] F. Zheng, P. Zhang, and W. Duan, *Comput. Phys. Commun.* **189**, 213 (2015).
- [22] M. Born and E. Wolf, *Principles of Optics: Electromagnetic Theory of Propagation, Interference and Diffraction of Light*, 7th ed. (Cambridge University Press, Cambridge, U.K., 1999), Chap. I, pp. 25–31.
- [23] J. Crank and P. Nicolson, *Math. Proc. Cambridge Philos. Soc.* **43**, 50 (1947).
- [24] X.-B. Bian, *Phys. Rev. A* **90**, 033403 (2014).
- [25] N. Yoshikawa, T. Tamaya, and K. Tanaka, *Science* **356**, 736 (2017).
- [26] X. Zhou, R. Lock, N. Wagner, W. Li, H. C. Kapteyn, and M. M. Murnane, *Phys. Rev. Lett.* **102**, 073902 (2009).
- [27] Y. S. You, M. Wu, Y. Yin, A. Chew, X. Ren, S. Gholam-Mirzaei, D. A. Browne, M. Chini, Z. Chang, K. J. Schafer, M. B. Gaarde, and S. Ghimire, *Opt. Lett.* **42**, 1816 (2017).
- [28] P. Antoine, B. Piraux, and A. Maquet, *Phys. Rev. A* **51**, R1750 (1995).
- [29] X.-M. Tong and Shih-I Chu, *Phys. Rev. A* **61**, 021802(R) (2000).
- [30] C. Chandre, S. Wiggins, and T. Uzer, *Physica D* **181**, 171 (2003).
- [31] F. H. M. Faisal and J. Z. Kamiński, *Phys. Rev. A* **56**, 748 (1997).
- [32] U. Saalmann, S. K. Giri, and J. M. Rost, *Phys. Rev. Lett.* **121**, 153203 (2018).
- [33] J.-Z. Jin, H. Liang, X.-R. Xiao, M.-X. Wang, S.-G. Chen, X.-Y. Wu, Q. Gong, and L.-Y. Peng, *Phys. Rev. A* **100**, 013412 (2019).
- [34] D. A. Sholl and J. A. Steckel, *Density Functional Theory, a Practical Introduction* (Wiley, New York, 2009).
- [35] J. Mayer, K. Khairy, and J. Howard, *Am. J. Phys.* **78**, 648 (2010).